

Half-quantum vortex state in a spin-orbit coupled Bose-Einstein condensate

B. Ramachandhran¹, Bogdan Opanchuk², Xia-Ji Liu², Han Pu¹, Peter D. Drummond², and Hui Hu²

¹*Department of Physics and Astronomy, and Rice Quantum Institute, Rice University, Houston, TX 77251, USA*

²*ARC Centres of Excellence for Quantum-Atom Optics and Centre for Atom Optics and Ultrafast Spectroscopy, Swinburne University of Technology, Melbourne 3122, Australia*

(Dated: January 9, 2012)

We investigate theoretically the condensate state and collective excitations of a two-component Bose gas in two-dimensional harmonic traps subject to isotropic Rashba spin-orbit coupling. In the weakly interacting regime when the inter-species interaction is larger than the intra-species interaction ($g_{\uparrow\downarrow} > g$), we find that the condensate ground state has a half-quantum-angular-momentum vortex configuration with spatial rotational symmetry and skyrmion-type spin texture. Upon increasing the interatomic interaction beyond a threshold g_c , the ground state starts to involve higher-order angular momentum components and thus breaks the rotational symmetry. In the case of $g_{\uparrow\downarrow} < g$, the condensate becomes unstable towards the superposition of two degenerate half-quantum vortex states. Both instabilities (at $g > g_c$ and $g_{\uparrow\downarrow} < g$) can be determined by solving the Bogoliubov equations for collective density oscillations of the half-quantum vortex state, and by analyzing the softening of mode frequencies. We present the phase diagram as functions of the interatomic interactions and the spin-orbit coupling. In addition, we directly simulate the time-dependent Gross-Pitaevskii equation to examine the dynamical properties of the system. Finally, we investigate the stability of the half-quantum vortex state against both the trap anisotropy and anisotropy in the spin-orbit coupling term.

PACS numbers: 05.30.Jp, 03.75.Mn, 67.85.Fg, 67.85.Jk

I. INTRODUCTION

Owing to the unprecedented control in interatomic interaction, geometry and purity, atomic quantum gases have proven to be an ideal many-body platform for exploring fundamental quantum states, such as Bose-Einstein condensates (BEC) [1], strongly interacting unitary Fermi superfluids [2, 3] and Mott-insulating states [4]. One of the latest achievement concerns the spin-orbit (SO) coupling in an ultracold spinor Bose gas of ⁸⁷Rb atoms [5], induced by the so-called “synthetic non-Abelian gauge fields”. Novel quantum states may be anticipated in the presence of SO coupling [6–18]. Indeed, for a homogeneous SO coupled spin-1/2 Bose gas with intra- and inter-species interactions (g and $g_{\uparrow\downarrow}$), a single plane-wave or a density-stripe condensate state has been predicted [8], depending on whether g is smaller or larger than $g_{\uparrow\downarrow}$. Interesting density patterns have been observed in the theoretical simulations for an SO coupled spinor condensate, in the absence [8, 11, 12, 17, 18] or presence [14–16] of rotation. The phenomenon of self-trapped BECs has also been proposed, in particular, in one-dimensional (1D) geometry [7].

In this work, we show that in a Rashba SO coupled, weakly interacting spin-1/2 Bose gas in two-dimensional (2D) harmonic traps, all bosons may condense into a non-trivial half-integer angular momentum state (or a half-quantum vortex state) with a skyrmion-type spin texture. We solve the mean-field Gross-Pitaevskii equation (GPE) for its density distributions and spin textures, and obtain its collective excitation spectrum by solving the Bogoliubov equation and by directly simulating real-time propagation of the GPE ground state under perturbation. The condensation of an SO coupled spin-1/2

Bose gas into a half-quantum vortex configuration was first suggested by Congjun Wu and co-workers in 2008 and its existence was discussed under the condition that the interaction is SU(2) symmetric, i.e., $g = g_{\uparrow\downarrow}$ [13]. Here, we explore systematically the parameter space for the half-quantum vortex state and analyze its stability. We present a phase diagram for the half-quantum vortex state as functions of the SO coupling and the interatomic interaction strengths. We also investigate the dynamical properties of the half-quantum vortex state by directly simulating the time-dependent GPE. Finally, the stability of the half-quantum vortex state against both the trap anisotropy and anisotropy in the spin-orbit coupling term is examined.

Our main results are summarized in Fig. 1. The half-quantum vortex state (the phase I) is the ground state if the intra-species interaction is smaller than the inter-species interaction ($g < g_{\uparrow\downarrow}$) and if the interaction strength is below a threshold ($g < g_c$). Otherwise, it becomes energetically unstable towards a superposition state of two degenerate half-quantum vortex states (the phase IIA), or a state involving higher-order angular momentum components (the phase IIB). With decreasing the dimensionless SO coupling strength λ_{SO} , the threshold g_c becomes exponentially large, leading to a large parameter space for the half-quantum vortex state (see Fig. 14). It is therefore feasible to be observed in the current experiments with ultracold SO coupled spinor Bose gases of ⁸⁷Rb atoms.

The rest of the paper is organized as follows. In the next section, we outline the model Hamiltonian and discuss briefly the existence of half-quantum vortex state in the non-interacting limit. In Sec. III, we present the numerical procedure of solving the GPE and Bogoliubov

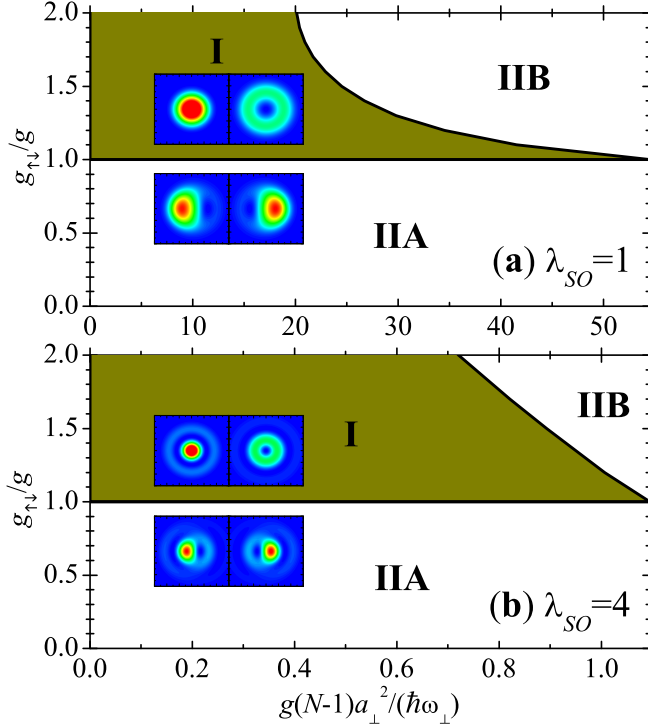


Figure 1: (color online). Phase diagram at two dimensionless SO coupling strengths, $\lambda_{SO} = 1$ (a) and $\lambda_{SO} = 4$ (b). The half-quantum vortex state (the phase I) becomes unstable when the intra-species interaction is larger than the inter-species interaction ($g > g_{\uparrow\downarrow}$, the phase IIA) or when the interatomic interactions are sufficient strong ($g > g_c$, the phase IIB). The insets show the density patterns of the spin-up and spin-down bosons in the phases I and IIA. We note that, the critical interaction strength g_c increases rapidly with decreasing the SO coupling strength λ_{SO} .

equations and discuss the typical density distributions and collective mode behaviors of the half-quantum vortex state. The collective excitation spectrum obtained from the Bogoliubov equation is compared to a direct simulation of the time-dependent GPE. In Sec. IV, we analyze the stability of the half-quantum vortex state by monitoring the softening of collective mode frequencies and by comparing the energy with that of some competing states. The phase diagram is then constructed as functions of interatomic interactions and SO coupling. The stability against the anisotropy in trapping potential and in spin-orbit coupling term is also carefully examined. Finally, we summarize in Sec. V and give some concluding

remarks.

II. THEORETICAL FRAMEWORK

We consider a two-component Bose gas confined in a 2D isotropic harmonic trap $V(\rho) = M\omega_{\perp}^2(x^2 + y^2)/2 = M\omega_{\perp}^2\rho^2/2$ with a Rashba SO coupling $\mathcal{V}_{SO} = -i\lambda_R(\hat{\sigma}_x\partial_y - \hat{\sigma}_y\partial_x)$, where λ_R is the Rashba SO coupling strength and $\hat{\sigma}_x$, $\hat{\sigma}_y$, and $\hat{\sigma}_z$ are the 2×2 Pauli matrices. The model Hamiltonian $\mathcal{H} = \int d\mathbf{r}[\mathcal{H}_0 + \mathcal{H}_{\text{int}}]$ is given by,

$$\mathcal{H}_0 = \Psi^\dagger \left[-\frac{\hbar^2 \nabla^2}{2M} + V(\rho) + \mathcal{V}_{SO} - \mu \right] \Psi, \quad (1)$$

$$\mathcal{H}_{\text{int}} = (g/2) \sum_{\sigma=\uparrow,\downarrow} \Psi_\sigma^\dagger \Psi_\sigma^\dagger \Psi_\sigma \Psi_\sigma + g_{\uparrow\downarrow} \Psi_\uparrow^\dagger \Psi_\uparrow \Psi_\downarrow^\dagger \Psi_\downarrow, \quad (2)$$

where $\mathbf{r} = (x, y)$ and $\Psi = [\Psi_\uparrow(\mathbf{r}), \Psi_\downarrow(\mathbf{r})]^T$ denotes the spinor Bose field operators in a collective way, and the chemical potential μ is to be determined by the total number of bosons N , i.e., $\int d\mathbf{r} \Psi^\dagger \Psi = N$. For simplicity, we have assumed equal intra-species interaction strength $g_{\uparrow\uparrow} = g_{\downarrow\downarrow} = g$. In experiments, the two-dimensionality can be readily realized by imposing a strong harmonic potential $V(z) = M\omega_z^2 z^2/2$ along axial direction, in such a way that $\mu, k_B T \ll \hbar\omega_z$ [19]. For the realistic case of ^{87}Rb atoms, the interaction strengths can be calculated from the two s -wave scattering lengths $a \simeq 100a_B$ and $a_{\uparrow\downarrow}$, using $g = \sqrt{8\pi}(\hbar^2/M)(a/a_z)$ and $g_{\uparrow\downarrow} = \sqrt{8\pi}(\hbar^2/M)(a_{\uparrow\downarrow}/a_z)$, respectively. Here $a_z = \sqrt{\hbar/(M\omega_z)}$ is the characteristic oscillator length in z -direction.

For a weakly interacting Bose gas at zero temperature, we assume that all the bosons condense into a single quantum state $\Phi(\mathbf{r}) = [\Phi_\uparrow(\mathbf{r}), \Phi_\downarrow(\mathbf{r})]^T$. Following the standard mean-field theory [20], we separate the field operator into a condensate and a fluctuation part, $\Psi_\sigma(\mathbf{r}) = \Phi_\sigma(\mathbf{r}) + \tilde{\Psi}_\sigma(\mathbf{r})$. Keeping up to the quadratic terms in $\tilde{\Psi}_\sigma(\mathbf{r})$, this separation leads to $\mathcal{H} = \int d\mathbf{r}[\mathcal{H}_{\text{GP}} + \mathcal{H}_T]$, where the condensate part is given by,

$$\mathcal{H}_{\text{GP}} = \Phi^\dagger [\mathcal{H}_{\text{osc}} + \mathcal{V}_{SO} - \mu] \Phi + \frac{g}{2} (|\Phi_\uparrow|^4 + |\Phi_\downarrow|^4) + g_{\uparrow\downarrow} |\Phi_\uparrow \Phi_\downarrow|^2, \quad (3)$$

and the fluctuation part $\mathcal{H}_T = \tilde{\Psi}^\dagger \mathcal{H}_{\text{Bog}} \tilde{\Psi}$ with

$$\mathcal{H}_{\text{Bog}} = \begin{bmatrix} \mathcal{H}_{s\uparrow} + g|\Phi_\uparrow|^2 & V_{\text{so}} + g_{\uparrow\downarrow}\Phi_\uparrow\Phi_\downarrow^* & g\Phi_\uparrow^2 & g_{\uparrow\downarrow}\Phi_\uparrow\Phi_\downarrow \\ V_{\text{so}}^\dagger + g_{\uparrow\downarrow}\Phi_\uparrow^*\Phi_\downarrow & \mathcal{H}_{s\downarrow} + g|\Phi_\downarrow|^2 & g_{\uparrow\downarrow}\Phi_\uparrow\Phi_\downarrow & g\Phi_\downarrow^2 \\ g(\Phi_\uparrow^*)^2 & g_{\uparrow\downarrow}\Phi_\uparrow^*\Phi_\downarrow^* & \mathcal{H}_{s\uparrow} + g|\Phi_\uparrow|^2 & -V_{\text{so}}^\dagger + g_{\uparrow\downarrow}\Phi_\uparrow^*\Phi_\downarrow \\ g_{\uparrow\downarrow}\Phi_\uparrow^*\Phi_\downarrow^* & g(\Phi_\downarrow^*)^2 & -V_{\text{so}} + g_{\uparrow\downarrow}\Phi_\uparrow\Phi_\downarrow^* & \mathcal{H}_{s\downarrow} + g|\Phi_\downarrow|^2 \end{bmatrix}. \quad (4)$$

Here $\mathcal{H}_{\text{osc}} \equiv -\hbar^2 \nabla^2 / (2M) + V(\rho)$, $\mathcal{H}_{s_\uparrow} \equiv \mathcal{H}_{\text{osc}} + g|\Phi_\uparrow|^2 + g_{\uparrow\downarrow}|\Phi_\downarrow|^2 - \mu$ and $\mathcal{H}_{s_\downarrow} \equiv \mathcal{H}_{\text{osc}} + g_{\uparrow\downarrow}|\Phi_\uparrow|^2 + g|\Phi_\downarrow|^2 - \mu$, $V_{\text{so}} \equiv -i\lambda_R(\partial_y + i\partial_x)$ and $V_{\text{so}}^\dagger \equiv -i\lambda_R(\partial_y - i\partial_x)$, and we have introduced a 4×4 Nambu spinor $\tilde{\Psi} = [\tilde{\Psi}_\uparrow(\mathbf{r}), \tilde{\Psi}_\downarrow(\mathbf{r}), \tilde{\Psi}_\uparrow^\dagger(\mathbf{r}), \tilde{\Psi}_\downarrow^\dagger(\mathbf{r})]^T$.

The condensate wave-function can be obtained from the GP equations $\delta\mathcal{H}_{\text{GP}}/\delta\Phi(\mathbf{r}) = 0$ [20], or explicitly,

$$\begin{bmatrix} \mathcal{H}_{s_\uparrow} & -i\lambda_R(\partial_y + i\partial_x) \\ -i\lambda_R(\partial_y - i\partial_x) & \mathcal{H}_{s_\downarrow} \end{bmatrix} \begin{bmatrix} \Phi_\uparrow(\mathbf{r}) \\ \Phi_\downarrow(\mathbf{r}) \end{bmatrix} = 0. \quad (5)$$

At zero temperature, we assume a single condensate state with *zero* quantum depletion, so that the condensate wave-function is normalized by $\int d\mathbf{r} [|\Phi_\uparrow|^2 + |\Phi_\downarrow|^2] = N$, where N is the total number of bosons. The equation becomes simplified if we write $\Phi_\uparrow = N^{1/2}\phi_\uparrow$ and $\Phi_\downarrow = N^{1/2}\phi_\downarrow$ and use accordingly the interaction strengths $g(N-1)$ and $g_{\uparrow\downarrow}(N-1)$. The normalization condition becomes $\int d\mathbf{r} [|\phi_\uparrow|^2 + |\phi_\downarrow|^2] = 1$.

The quasi-particle wave-functions with energy $\hbar\omega$ satisfy the Bogoliubov equations [20],

$$\mathcal{H}_{\text{Bog}} \begin{bmatrix} u_\uparrow(\mathbf{r}) \\ u_\downarrow(\mathbf{r}) \\ v_\uparrow(\mathbf{r}) \\ v_\downarrow(\mathbf{r}) \end{bmatrix} = \hbar\omega \begin{bmatrix} +u_\uparrow(\mathbf{r}) \\ +u_\downarrow(\mathbf{r}) \\ -v_\uparrow(\mathbf{r}) \\ -v_\downarrow(\mathbf{r}) \end{bmatrix}, \quad (6)$$

and is normalized by $\int d\mathbf{r} [|u_\uparrow|^2 + |u_\downarrow|^2 - |v_\uparrow|^2 - |v_\downarrow|^2] = 1$. These Bogoliubov quasi-particles correspond to the different collective density oscillation modes around the condensate with the frequency ω [21]. It is easy to see that the wave-function $[v_\uparrow^*(\mathbf{r}), v_\downarrow^*(\mathbf{r}), u_\uparrow^*(\mathbf{r}), u_\downarrow^*(\mathbf{r})]^T$ is also a solution of Eq. (6), but with energy $-\hbar\omega$. This is anticipated for the usual Bogoliubov transformation. Physically, we should restrict to a non-negative mode frequency, $\omega \geq 0$.

In harmonic traps, it is natural to use the trap units, i.e. to take $\hbar\omega_\perp$ as the unit for energy and the harmonic oscillator length $a_\perp = \sqrt{\hbar/(M\omega_\perp)}$ as the unit for length. This is equivalent to set $\hbar = k_B = M = \omega_\perp = 1$. For the SO coupling, we introduce an SO coupling length $a_\lambda = \hbar^2/(M\lambda_R)$ and consequently define a dimensionless SO coupling strength $\lambda_{SO} = a_\perp/a_\lambda = \sqrt{(M/\hbar^3)\lambda_R/\omega_\perp}$. In an SO coupled spin-1/2 BEC of ^{87}Rb atoms as realized recently by the NIST group [5], λ_{SO} is about 10. In the typical experiment for 2D spin-1/2 ^{87}Rb BECs [19], the interatomic interaction strengths are about $g(N-1) \approx g_{\uparrow\downarrow}(N-1) = 10^2 \sim 10^3 \hbar\omega_\perp/a_\perp^2$. These coupling strengths, however, can be precisely tuned by properly choosing the parameters of the laser fields that lead to the harmonic confinement and the SO coupling.

A. Single-particle solutions

The appearance of the half-quantum vortex state may be easily understood in the non-interacting limit [13].

In the absence of interatomic interactions, the single-particle wave-function $[\phi_\uparrow(\mathbf{r}), \phi_\downarrow(\mathbf{r})]^T$ with energy ϵ is given by,

$$\begin{bmatrix} \mathcal{H}_{\text{osc}} & -i\lambda_R(\partial_y + i\partial_x) \\ -i\lambda_R(\partial_y - i\partial_x) & \mathcal{H}_{\text{osc}} \end{bmatrix} \begin{bmatrix} \phi_\uparrow \\ \phi_\downarrow \end{bmatrix} = \epsilon \begin{bmatrix} \phi_\uparrow \\ \phi_\downarrow \end{bmatrix}. \quad (7)$$

In polar coordinates (ρ, φ) , we have $-i(\partial_y \pm i\partial_x) = e^{\mp i\varphi}[\pm\partial/\partial\rho - (i/\rho)\partial/\partial\varphi]$. Because of the isotropic harmonic potential $V(\rho)$, the single-particle wave-function may have a well-defined azimuthal angular momentum $l_z = m$ and may take the form,

$$\phi_m(\mathbf{r}) = \begin{bmatrix} \phi_\uparrow(\rho) \\ \phi_\downarrow(\rho)e^{i\varphi} \end{bmatrix} \frac{e^{im\varphi}}{\sqrt{2\pi}}. \quad (8)$$

This state also has a well-defined total angular momentum $j_z = l_z + s_z = m + 1/2$. In general, we may denote the energy spectrum as ϵ_{nm} , where $n = (0, 1, 2, \dots)$ is the quantum number for the transverse (radial) direction. There is an interesting two-fold degeneracy of the energy spectrum: any eigenstate $\phi(\mathbf{r}) = [\phi_\uparrow(\mathbf{r}), \phi_\downarrow(\mathbf{r})]^T$ is degenerate with its time-reversal partner $\mathcal{T}\phi(\mathbf{r}) \equiv (i\sigma_y \mathcal{C})\phi(\mathbf{r}) = [\phi_\downarrow^*(\mathbf{r}), -\phi_\uparrow^*(\mathbf{r})]^T$. Here \mathcal{C} is the complex conjugate operation. This Kramer doublet is the direct consequence of the time-reversal symmetry satisfied by the model Hamiltonian. It preserves as well in the presence of interatomic interactions. As a result, we may restrict the quantum number m to be non-negative integers, as a negative m can always be regarded as the time-reversal partner for a state with $m \geq 0$.

To solve numerically the single-particle spectrum, we adopt a basis-expansion method. To this end, we expand first,

$$\phi_\uparrow(\rho) = \sum_k A_k R_{km}(\rho), \quad (9)$$

$$\phi_\downarrow(\rho) = \sum_k B_k R_{km+1}(\rho), \quad (10)$$

where

$$R_{km} = \frac{1}{a_\perp} \sqrt{\frac{2k!}{(k+|m|)!}} \left(\frac{\rho}{a_\perp}\right)^{|m|} e^{-\frac{\rho^2}{2a_\perp^2}} \mathcal{L}_k^{|m|}\left(\frac{\rho^2}{a_\perp^2}\right) \quad (11)$$

is the radial wave-function of a 2D harmonic oscillator \mathcal{H}_{osc} with energy $(2k+|m|+1)\hbar\omega_\perp$, and $\mathcal{L}_k^{|m|}$ is the associated Legendre polynomial. Then, we have the following secular matrix,

$$\begin{bmatrix} \mathcal{H}_{\text{osc}\uparrow} & \mathcal{M}^T \\ \mathcal{M} & \mathcal{H}_{\text{osc}\downarrow} \end{bmatrix} \begin{bmatrix} A_k \\ B_k \end{bmatrix} = \epsilon \begin{bmatrix} A_k \\ B_k \end{bmatrix}, \quad (12)$$

where the matrix elements are given by (for $m \geq 0$)

$$\begin{aligned} \mathcal{H}_{\text{osc}\uparrow, kk'} &= \hbar\omega_\perp [2k+m+1] \delta_{kk'}, \\ \mathcal{H}_{\text{osc}\downarrow, kk'} &= \hbar\omega_\perp [2k+(m+1)+1] \delta_{kk'}, \\ \mathcal{M}_{kk'} &= \hbar\omega_\perp \lambda_{SO} \left[\sqrt{k'+m+1} \delta_{kk'} + \sqrt{k'} \delta_{kk'-1} \right]. \end{aligned}$$

Diagonalization of the secular matrix Eq. (12) leads to the single-particle spectrum and single-particle wavefunctions. In numerical calculations, it is necessary to impose a cut-off k_{\max} for the radial quantum number k of the 2D harmonic oscillator. For $\lambda_{SO} \leq 20$, we find that $k_{\max} = 256$ is already sufficiently large to have an accurate energy spectrum. With this cut-off, the dimension of the secular matrix in Eq. (12) is $2k_{\max} = 512$.

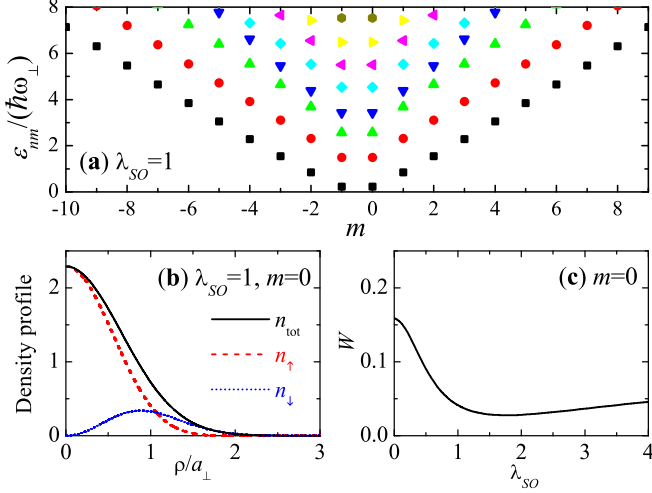


Figure 2: (color online). (a) Single-particle energy spectrum at $\lambda_{SO} = 1$. (b) The density profiles for the single-particle state with $m = 0$ at $\lambda_{SO} = 1$. (c) The W -function for the $m = 0$ single-particle state as a function of SO coupling strength. It is always positive at arbitrary SO coupling strength.

In Fig. 2a, we show the single-particle energy spectrum at $\lambda_{SO} = 1$. For arbitrary SO interaction strength, we find numerically that the doublet single-particle ground state always occurs at $m = 0$ (or $m = -1$ for its time-reversal partner state).

B. Appearance of the half-quantum vortex state

The single-particle state with $m = 0$, $\phi_0(\mathbf{r}) = [\phi_\uparrow(\rho), \phi_\downarrow(\rho)e^{i\varphi}]^T / \sqrt{2\pi}$, has a half-quantum vortex configuration [13, 22], as the spin-up component stays in the s -state while the spin-down component in the p -state and the resulting spin texture is of skyrmion type (see Fig. 2b for density distributions and Sec. IIIB for more discussions on spin-texture). In the absence of interactions, however, there is a degenerate time-reversal state, $\mathcal{T}\phi_0(\mathbf{r}) = [\phi_\downarrow(\rho)e^{-i\varphi}, -\phi_\uparrow(\rho)]^T / \sqrt{2\pi}$, which is also a half-quantum vortex state. Therefore, in general, the ground single-particle state is a superposition of two degenerate half-quantum vortex states of $\phi_0(\mathbf{r})$ and $\mathcal{T}\phi_0(\mathbf{r})$, which takes the form $\phi_s(\mathbf{r}) = \alpha\phi_0(\mathbf{r}) + \beta\mathcal{T}\phi_0(\mathbf{r})$, or explicitly,

$$\phi_s(\mathbf{r}) = \frac{1}{\sqrt{2\pi}} \begin{bmatrix} \alpha\phi_\uparrow(\rho) + \beta\phi_\downarrow(\rho)e^{-i\varphi} \\ \alpha\phi_\downarrow(\rho)e^{i\varphi} - \beta\phi_\uparrow(\rho) \end{bmatrix}. \quad (13)$$

Here α and β are two arbitrary complex numbers satisfying $|\alpha|^2 + |\beta|^2 = 1$.

In the presence of very weak interatomic interactions such that $g(N-1)a_\perp^2, g_{\uparrow\downarrow}(N-1)a_\perp^2 \ll \Delta\epsilon$, where $\Delta\epsilon$ is the energy difference between the single-particle ground state $\phi_0(\mathbf{r})$ and the first excited state $\phi_1(\mathbf{r})$, we may determine the superposition coefficients α and β by minimizing the GP energy, $E_{\text{GP}}[\phi_s(\mathbf{r})] = \int d\mathbf{r} \mathcal{H}_{\text{GP}}[\phi_s(\mathbf{r})]$. After a simple algebra, we find that,

$$\Delta E = E_{\text{GP}}[\phi_s(\mathbf{r})] - E_{\text{GP}}[\phi_0(\mathbf{r})], \quad (14)$$

$$= (g_{\uparrow\downarrow} - g)(N-1)|\alpha\beta|^2 W[\phi_0(\mathbf{r})], \quad (15)$$

where the W -function is given by,

$$W[\phi(\mathbf{r})] = \int d\mathbf{r} [(|\phi_\uparrow|^2 - |\phi_\downarrow|^2)^2 - 2\phi_\uparrow^2\phi_\downarrow^2]. \quad (16)$$

Therefore, a half-quantum vortex state is preferable if $(g_{\uparrow\downarrow} - g)W > 0$. Otherwise, an equal-weight superposition of two degenerate half-quantum vortex states with $|\alpha| = |\beta| = 1/\sqrt{2}$ will be the ground state. As shown in Fig. 2c, the W -function for $\phi_0(\mathbf{r})$ is positive for arbitrary SO coupling. We thus conclude that a half-quantum vortex state should appear at weak interatomic interactions provided that the inter-species interaction is larger than the intra-species interaction ($g_{\uparrow\downarrow} > g$).

III. DENSITY DISTRIBUTIONS AND COLLECTIVE EXCITATIONS

Let us now consider finite interatomic interactions, by solving the GPE for density distributions and spin-textures, and the Bogoliubov equation for the collective density excitations.

A. GPE solutions of the half-quantum vortex state

For the half-quantum vortex condensate state with $m = 0$, the GP equation becomes $\mathcal{L}_{\text{GP}}[\phi_\uparrow(\rho), \phi_\downarrow(\rho)] = 0$, where

$$\mathcal{L}_{\text{GP}} = \begin{bmatrix} \mathcal{H}_{s,0} + \bar{g}\phi_\uparrow^2 + \bar{g}_{\uparrow\downarrow}\phi_\downarrow^2 & \lambda_R(\partial_\rho + 1/\rho) \\ \lambda_R(-\partial_\rho) & \mathcal{H}_{s,1} + \bar{g}_{\uparrow\downarrow}\phi_\uparrow^2 + \bar{g}\phi_\downarrow^2 \end{bmatrix}, \quad (17)$$

$\bar{g} \equiv g(N-1)/(2\pi)$ and $\bar{g}_{\uparrow\downarrow} \equiv g_{\uparrow\downarrow}(N-1)/(2\pi)$, and $\mathcal{H}_{s,m} \equiv -[\hbar^2/(2M)][\partial^2/\partial\rho^2 + (1/\rho)\partial_\rho - m^2/\rho^2] + V(\rho) - \mu$. The numerical procedure for solving GPE is very similar to that for single-particle states in Eq. (12). We expand $\phi_\uparrow(\rho) = \sum_k A_k R_{k0}(\rho)$ and $\phi_\downarrow(\rho) = \sum_k B_k R_{k1}(\rho)$, and obtain the secular matrix (with $m = 0$),

$$\begin{bmatrix} \mathcal{H}_{\text{osc}\uparrow} + \mathcal{I}_\uparrow & \mathcal{M}^T \\ \mathcal{M} & \mathcal{H}_{\text{osc}\downarrow} + \mathcal{I}_\downarrow \end{bmatrix} \begin{bmatrix} A_k \\ B_k \end{bmatrix} = \mu \begin{bmatrix} A_k \\ B_k \end{bmatrix}, \quad (18)$$

where

$$\mathcal{I}_{\uparrow,kk'} = \int_0^\infty \rho d\rho R_{k0}(\rho) (\bar{g}\phi_\uparrow^2 + \bar{g}\downarrow\phi_\downarrow^2) R_{k'0}(\rho), \quad (19)$$

$$\mathcal{I}_{\downarrow,kk'} = \int_0^\infty \rho d\rho R_{k1}(\rho) (\bar{g}\downarrow\phi_\uparrow^2 + \bar{g}\phi_\downarrow^2) R_{k'1}(\rho). \quad (20)$$

The chemical potential is given by the lowest eigenvalue of the secular matrix. Due to the non-linear terms of $\mathcal{I}_{\uparrow,kk'}$ and $\mathcal{I}_{\downarrow,kk'}$, we have to update the condensate wave-functions and densities iteratively. To overcome the large non-linearity, we use a simple mixing scheme by setting a small parameter $0 < \gamma < 1$ and replace the previous density $\phi_{\sigma,old}^2$ by $(1 - \gamma)\phi_{\sigma,old}^2 + \gamma\phi_\sigma^2$, where ϕ_σ^2 is the density calculated in the current step [23]. The choice of γ depends on the interaction strengths. It becomes smaller for larger \bar{g} and $\bar{g}\downarrow$. We run the iteration until convergence is achieved within a set tolerance. We have checked that this procedure of solving GPE is stable for interaction strengths up to $g(N-1), g\downarrow(N-1) < 10^3 \hbar\omega_\perp/a_\perp^2$. For even larger non-linearity, it seems to be impractical to expand the condensate wave-function using the 2D harmonic oscillator basis. Therefore for large interaction strengths, we use a time-splitting spectral method (TSSP) technique to solve the coupled GP equations and obtain the ground state by imaginary-time propagation [24, 25]. For small interaction strengths, results obtained from TSSP are identical to those obtained from the basis-expansion method.

B. Density distributions and spin textures

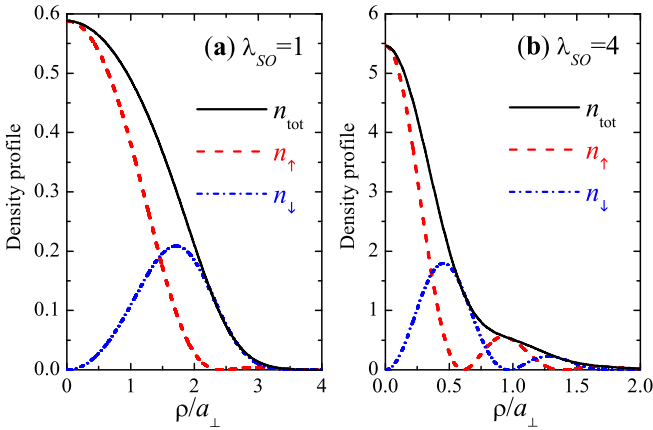


Figure 3: (color online). Density distributions at $\lambda_{SO} = 1$ and $g(N-1) = 40\hbar\omega_\perp/a_\perp^2$ (a) and at $\lambda_{SO} = 4$ and $g(N-1) = \hbar\omega_\perp/a_\perp^2$ (b). Here, the ratio $g\uparrow\downarrow/g = 1.1$.

In Fig. 3, we present the radial density distributions of the half-quantum vortex condensate state at two SO coupling strengths: $\lambda_{SO} = 1$ and $\lambda_{SO} = 4$. The increase of the SO coupling leads to more oscillations in the radial direction. By comparing Fig. 3(a) with Fig. 2(b), one finds

that the density distributions are flattened significantly by interatomic interactions, as anticipated. The 2D contour plot of the spin-up and spin-down density patterns of the half-quantum vortex state is shown in the inset of Fig. 1 (in the phase I).

To gain more insights of the half-quantum vortex state, it is useful to calculate the spin vector

$$\mathbf{S}(\mathbf{r}) = \frac{1}{2} \frac{\Phi^\dagger \sigma \Phi}{|\Phi|^2} \quad (21)$$

and the skyrmion density

$$n_{\text{skyrmion}}(\mathbf{r}) = \frac{8}{4\pi} \mathbf{S} \cdot [\partial_x \mathbf{S} \times \partial_y \mathbf{S}]. \quad (22)$$

The skyrmion density is a measure of the winding of the spin profile. If it integrates to 1 or -1 , a topological stable knot exists in the spin texture.

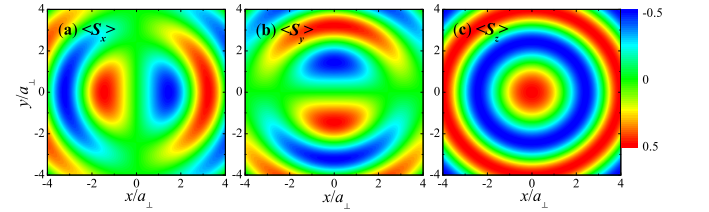


Figure 4: (color online). Contour plots of the three components of spin vector $\mathbf{S}(\mathbf{r})$ at $\lambda_{SO} = 1$, $g(N-1) = 40\hbar\omega_\perp/a_\perp^2$ and $g\uparrow\downarrow/g = 1.1$.

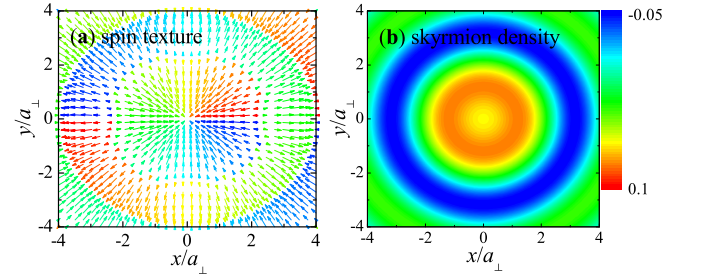


Figure 5: (color online) (a) Two-dimensional vector plot of the transverse spin vector (S_x, S_y) at $\lambda_{SO} = 1$, $g(N-1) = 40\hbar\omega_\perp/a_\perp^2$ and $g\uparrow\downarrow/g = 1.1$. The color and length of arrows give respectively the orientation and the magnitude of (S_x, S_y) . (b) The corresponding skyrmion density $n_{\text{skyrmion}}(\mathbf{r})$.

In Fig. 4, we report the three components of the spin vector at $\lambda_{SO} = 1$, $g(N-1) = 40\hbar\omega_\perp/a_\perp^2$ and $g\uparrow\downarrow/g = 1.1$. The transverse spin texture is shown in Fig. 5a by arrows, with color and length representing the orientation and the magnitude of the transverse spin vector (S_x, S_y) , respectively. It is readily seen that the spin vector spirals in space and form a skyrmion-type texture. Quantitatively, this is most clearly illustrated in Fig. 5b, where we plot the skyrmion density.

C. Solutions of Bogoliubov equations

Given the wave-function of the half-quantum vortex state, $[\phi_\uparrow(\rho), \phi_\downarrow(\rho) e^{i\varphi}]^T / \sqrt{2\pi}$, we now turn to consider its collective excitations, as described by the coupled Bogoliubov equations (6). As a result of rotational symmetry, it is easy to see that, the Bogoliubov wave-functions have a good azimuthal quantum number m and can be written as, $[u_\uparrow(\rho), u_\downarrow(\rho) e^{i\varphi}, v_\uparrow(\rho), v_\downarrow(\rho) e^{-i\varphi}]^T e^{im\varphi} / \sqrt{2\pi}$. Therefore, we have

$$\mathcal{H}_{\text{Bog}} \begin{bmatrix} u_\uparrow(\rho) \\ u_\downarrow(\rho) \\ v_\uparrow(\rho) \\ v_\downarrow(\rho) \end{bmatrix} = \hbar\omega \begin{bmatrix} +u_\uparrow(\rho) \\ +u_\downarrow(\rho) \\ -v_\uparrow(\rho) \\ -v_\downarrow(\rho) \end{bmatrix}, \quad (23)$$

where

$$\mathcal{H}_{\text{Bog}} = \begin{bmatrix} \mathcal{L}_m + \mathcal{U} & \mathcal{U} \\ \mathcal{U} & \mathcal{L}_{-m} + \mathcal{U} \end{bmatrix}, \quad (24)$$

with

$$\mathcal{L}_m = \begin{bmatrix} \mathcal{H}_{s,m} + \bar{g}\phi_\uparrow^2 + \bar{g}\phi_\downarrow^2 & \lambda_R [\partial_\rho + (m+1)/\rho] \\ \lambda_R (-\partial_\rho + m/\rho) & \mathcal{H}_{s,m+1} + \bar{g}\phi_\uparrow^2 + \bar{g}\phi_\downarrow^2 \end{bmatrix}, \quad (25)$$

and

$$\mathcal{U} = \begin{bmatrix} \bar{g}\phi_\uparrow^2 & \bar{g}\phi_\uparrow\phi_\downarrow \\ \bar{g}\phi_\uparrow\phi_\downarrow & \bar{g}\phi_\downarrow^2 \end{bmatrix}. \quad (26)$$

To solve the Bogoliubov equation, as before we expand the wave-functions using 2D harmonic oscillator basis,

$$u_\uparrow(\rho) = \sum_k a_k R_{km}(\rho), \quad (27)$$

$$u_\downarrow(\rho) = \sum_k b_k R_{k,m+1}(\rho), \quad (28)$$

$$v_\uparrow(\rho) = \sum_k c_k R_{km}(\rho), \quad (29)$$

$$v_\downarrow(\rho) = \sum_k d_k R_{k,m-1}(\rho). \quad (30)$$

This leads to a secular matrix of \mathcal{H}_{Bog} , whose elements can be calculated directly using the 2D harmonic oscillator basis. We note that, to obtain the Bogoliubov quasiparticles we cannot diagonalize directly the secular matrix, because of the minus sign before $v_\uparrow(\rho)$ and $v_\downarrow(\rho)$ at the right-hand side of Eq. (23). Instead, we should diagonalize a *non-symmetric* matrix $\text{Diag}\{+1, +1, -1, -1\} \mathcal{H}_{\text{Bog}}$ and normalize the quasiparticle wave-functions according to $\int_0^\infty \rho d\rho [u_\uparrow^2 + u_\downarrow^2 - v_\uparrow^2 - v_\downarrow^2] = 1$. The number of resulting eigenvalues is two times the number that we want. There are two branches of eigenvalues, one is positive and the other negative, as a result of the duality between the solution $[u_\uparrow(\mathbf{r}), u_\downarrow(\mathbf{r}), v_\uparrow(\mathbf{r}), v_\downarrow(\mathbf{r})]^T$ (with energy $+\hbar\omega$) and $[v_\uparrow^*(\mathbf{r}), v_\downarrow^*(\mathbf{r}), u_\uparrow^*(\mathbf{r}), u_\downarrow^*(\mathbf{r})]^T$ (with energy $-\hbar\omega$).

We should take the positive branch. We note also that the Bogoliubov quasi-particles at a negative azimuthal quantum number m may be obtained from the negative branch of the solution with $m > 0$, because of the duality.

1. Breathing modes

In the case of the breathing mode ($m = 0$), where

$$\mathcal{H}_{\text{Bog}} = \begin{bmatrix} \mathcal{L}_{\text{GP}} + \mathcal{U} & \mathcal{U} \\ \mathcal{U} & \mathcal{L}_{\text{GP}} + \mathcal{U} \end{bmatrix}, \quad (31)$$

we may have an alternative way to solve the Bogoliubov equation, following Hutchinson, Zaremba, and Griffin (HZG) [26]. By denoting collectively $u = [u_\uparrow(\rho), u_\downarrow(\rho)]$ and $v = [v_\uparrow(\rho), v_\downarrow(\rho)]$, we have,

$$(\mathcal{L}_{\text{GP}} + 2\mathcal{U})(u + v) = \hbar\omega(u - v), \quad (32)$$

$$\mathcal{L}_{\text{GP}}(u - v) = \hbar\omega(u + v). \quad (33)$$

Let us now expand the wave-functions $u \pm v$ in terms of the eigenfunctions ψ_α of \mathcal{L}_{GP} with energy ϵ_α (i.e., $\mathcal{L}_{\text{GP}}\psi_\alpha = \epsilon_\alpha\psi_\alpha$),

$$u - v = \sum_{\alpha \neq 0} \frac{c_\alpha}{\epsilon_\alpha^{1/2}} \psi_\alpha, \quad (34)$$

$$u + v = \sum_{\alpha \neq 0} \frac{\epsilon_\alpha^{1/2} c_\alpha}{\hbar\omega} \psi_\alpha. \quad (35)$$

Here, the lowest eigenstate of \mathcal{L}_{GP} with zero energy should be removed, as it corresponds exactly to the condensate mode. It is easy to see that $(\mathcal{L}_{\text{GP}} + 2\mathcal{U})\mathcal{L}_{\text{GP}}(u - v) = (\hbar\omega)^2(u - v)$ and $\mathcal{L}_{\text{GP}}(\mathcal{L}_{\text{GP}} + 2\mathcal{U})(u + v) = (\hbar\omega)^2(u + v)$. Inserting the expansion of $u - v$ or $u + v$, one finds the secular equation,

$$\sum_\beta \left\{ \epsilon_\alpha^2 \delta_{\alpha\beta} + 2\epsilon_\alpha^{1/2} \mathcal{U}_{\alpha\beta} \epsilon_\beta^{1/2} \right\} c_\beta = (\hbar\omega)^2 c_\alpha, \quad (36)$$

where

$$\mathcal{U}_{\alpha\beta} = \int_0^\infty \rho d\rho \psi_\alpha^\dagger(\rho) \mathcal{U} \psi_\beta(\rho). \quad (37)$$

By diagonalizing the secular matrix, one obtains the mode frequency ω and the coefficients c_α . The latter should be normalized as $\sum_\alpha c_\alpha^2 = \hbar\omega$, in accord with the normalization condition for u and v .

We have checked numerically that the HZG solution leads to exactly the same result as the direct diagonalization of the non-symmetric matrix $\text{Diag}\{+1, +1, -1, -1\} \mathcal{H}_{\text{Bog}}$, if we discard the zero-frequency condensate mode in the latter method.

D. Collective excitations

In Fig. 6, we report the breathing ($m = 0$) and the dipole mode ($m = \pm 1$) frequencies as a function of the

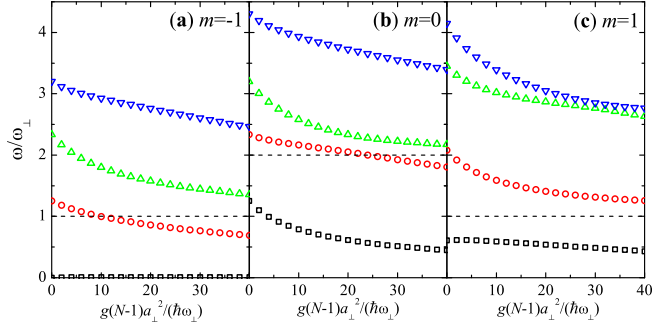


Figure 6: (color online). The mode frequency of breathing ($m = 0$) and dipole ($m = \pm 1$) modes as a function of interaction strength at a fixed SO coupling $\lambda_{SO} = 1$ and at $g_{\uparrow\downarrow} = 1.1g$.

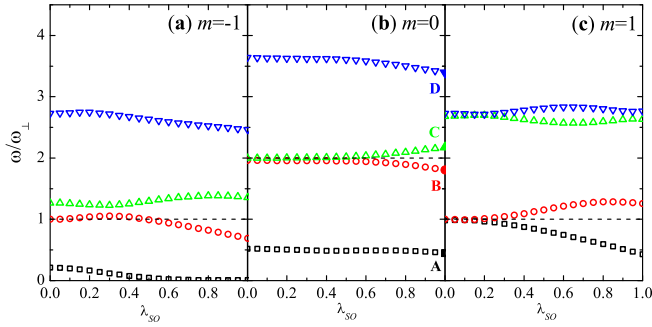


Figure 7: (color online). The mode frequency of breathing ($m = 0$) and dipole ($m = \pm 1$) modes as a function of SO coupling at a fixed interaction strength $g(N-1) = 40\hbar\omega_{\perp}/a_{\perp}^2$ and at $g_{\uparrow\downarrow} = 1.1g$.

interaction strength. With increasing interaction, the mode frequency decreases and seems to saturate at sufficiently large interactions. This may be anticipated from the point of view of two-fluid hydrodynamic behavior in the Thomas-Fermi regime. In Fig. 7, we report the dependence of the mode frequencies on SO coupling. In the absence of SO coupling, the breathing mode with $\omega = 2\omega_{\perp}$ and the dipole mode with $\omega = \omega_{\perp}$ are the exact solutions of quantum many-body systems in harmonic traps. At a finite SO coupling, however, we find that these two solutions are no longer exact. The relative deviations of the breathing mode and dipole mode at $\lambda_{SO} = 1$ are about 10% and 30%, respectively.

In Fig. 8, we plot the Bogoliubov wave-functions of the lowest four breathing modes at $\lambda_{SO} = 1$, $g(N-1) = 40\hbar\omega_{\perp}/a_{\perp}^2$ and $g_{\uparrow\downarrow} = 1.1g$. We find that the density response is mainly carried by $u_{\uparrow}(\rho)$ and $u_{\downarrow}(\rho)$ components. With increasing mode frequency, more and more nodes appear in $u_{\uparrow}(\rho)$ and $u_{\downarrow}(\rho)$. In contrast, the response in $v_{\uparrow}(\rho)$ and $v_{\downarrow}(\rho)$ is relatively weak and the curve shape is nearly unchanged as the mode frequency increases.

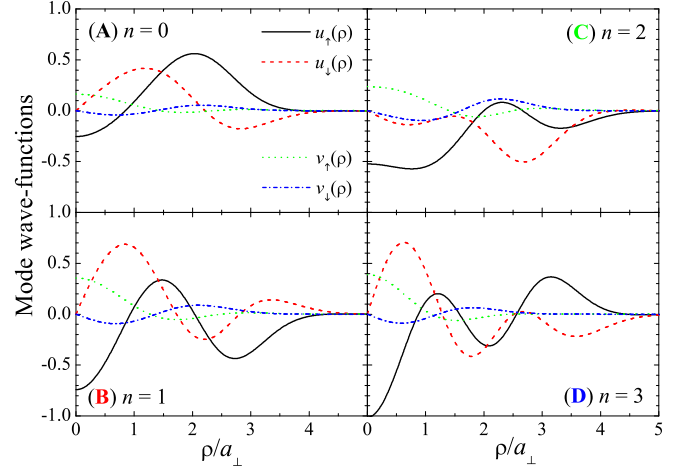


Figure 8: (color online). Bogoliubov wave-functions of the lowest four breathing modes at $\lambda_{SO} = 1$, $g(N-1) = 40\hbar\omega_{\perp}/a_{\perp}^2$ and $g_{\uparrow\downarrow} = 1.1g$. The mode frequencies are indicated in Fig. 7b by solid symbols.

E. Dynamical Calculations

To investigate the dynamical properties of the system, we also perform direct simulations of the system by real-time propagation of the ground state under perturbation. To do this, firstly we obtain the ground state by solving the coupled GP equations in Eqn. (3) using the TSSP technique. The half-quantum vortex ground state is perturbed in various ways. We observe that the mode frequencies obtained by dynamical simulation agree well with those obtained by solving Bogoliubov equations (shown in Fig. 6).

Breathing mode analysis, $m = 0$: We excite the monopole mode by weak relaxation of the trapping frequency at time $t = 0$, and letting the system propagate in real-time. As the breathing mode excitation is isotropic in x - y space, it is sufficient to observe the dynamic response of the collective coordinate along one axis, say, the x -axis. Here, we pick the mean square of the center-of-mass coordinate as the quantity of interest:

$$\langle x^2 \rangle_{\sigma} = \frac{\int |\phi_{\sigma}|^2 x^2 dx dy}{\int |\phi_{\sigma}|^2 dx dy},$$

where $\sigma = \uparrow, \downarrow$ -spin components. In Fig. 9 (a),(b), we plot the time response of $\langle x^2(t) \rangle_{\sigma}$ for a typical parameter set. In Fig. 9 (c),(d), we show the corresponding frequency response by plotting the single-sided amplitude spectrum $|\langle x^2(\omega) \rangle_{\sigma}|$, which are just the Fourier transforms of $\langle x^2(t) \rangle_{\sigma}$. We observe frequency peaks at $\omega/\omega_{\perp} \simeq 0.46, 1.8, 2.18$ and at 3.40 (not shown). We note that these values exactly match with the mode frequencies obtained for this parameter set by solving Bogoliubov equations, shown in Fig. 6(b).

Dynamical calculations also reveal the coupling between the center-of-mass motion and the internal spin degrees of freedom, a trademark signature of spin-orbit cou-

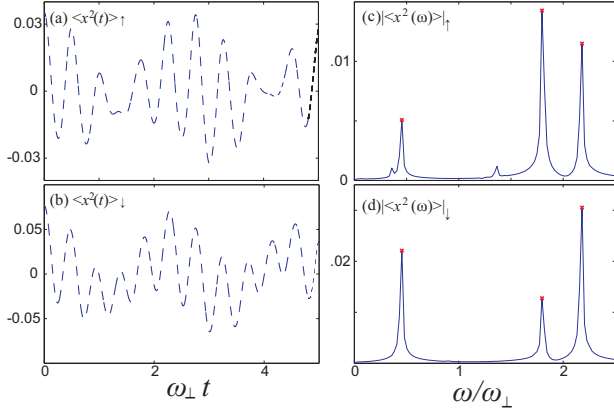


Figure 9: (color online). (a),(b): Dynamic response of the mean square of the center-of-mass coordinate in x -direction of \uparrow - and \downarrow - spin components respectively. We have shifted the curves by subtracting the time-averaged $\langle x^2(t) \rangle_\sigma$. Without this shift, the Fourier spectrum as shown in (c) and (d) will be dominated by a large peak at $\omega = 0$. (c),(d): Corresponding single-sided amplitude spectrum of the collective coordinate. Parameters used: $\lambda_{SO} = 1.0, g(N-1) = 40\hbar\omega_\perp/a_\perp^2, g_{\uparrow\downarrow}/g = 1.1$.

pled systems. We shall now discuss the dynamic response of the population difference $\Delta n = \int d\mathbf{r} (|\phi_\uparrow|^2 - |\phi_\downarrow|^2)$. In Fig. 10(a), we plot the time response of $\Delta n(t)$ for the same parameter set mentioned in Fig. 9. In Fig. 10(b), we show the corresponding frequency response by plotting the single-sided amplitude spectrum $|\Delta n(\omega)|$. We observe frequency peaks at $\omega/\omega_\perp \simeq 0.46, 1.8, 2.18$ and at 3.40 (not shown), exactly matching with the mode frequencies obtained in Fig. 9. This analysis clearly shows that the population transfer between the two spin components shares a similar dynamic response with the collective motional coordinate. In this aspect, response of Δn in a spin-orbit coupled spinor BEC (shown here) is similar to the effects observed in the presence of internal Josephson coupling in multi-component condensates [27].

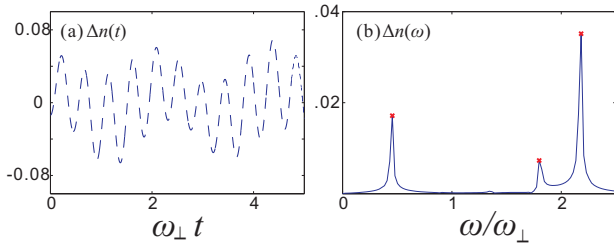


Figure 10: (color online). (a) Dynamic response and (b) single-sided amplitude spectrum of population difference Δn for the same parameter set used in Fig. 9.

Dipole mode analysis, $m = \pm 1$: We excite the dipole modes by displacing the trap in x -direction by a small amount at time $t = 0$, and letting the system propagate in real-time. We observe the dynamic response of the

center-of-mass coordinate in x -direction:

$$\langle x \rangle_\sigma = \frac{\int |\phi_\sigma|^2 x dx dy}{\int |\phi_\sigma|^2 dx dy}.$$

In Fig. 11 (a),(b), we plot the time response of this collective coordinate in x -direction of \uparrow - and \downarrow - spin components for a typical parameter set. In Fig. 11 (c),(d), we show the corresponding frequency response by plotting the single-sided amplitude spectrum $|\langle x(\omega) \rangle_\sigma|$. We observe frequency peaks at $\omega/\omega_\perp \simeq 0.05, 0.43, 0.70, 1.25, 1.34$, (shown) and at $2.5, 2.64, 2.76$ (not shown). We note that these values exactly agree the mode frequencies obtained for this parameter set by solving Bogoliubov equations, shown in Fig. 6(a),(c).

In the inset of Fig. 11(a), we show the dynamics of the center-of-mass coordinate. It is important to note that even though the trap is displaced only in the x -direction, we also observe a similar dynamic response in y -direction of both spin components (only \uparrow -spin component shown). This behavior occurs due to the vorticity induced by the spin-orbit coupling — the vortex state experiences a Magnus force that is perpendicular to its motion. Hence a displacement in the x -direction induces a motion along the y -direction. Furthermore, the trace of the center-of-mass and its magnitude are affected by the strength of the inter-particle interactions and the spin-orbit coupling induced population transfer, as observed in the case of the breathing mode excitation, between the \uparrow - and \downarrow - spin components.

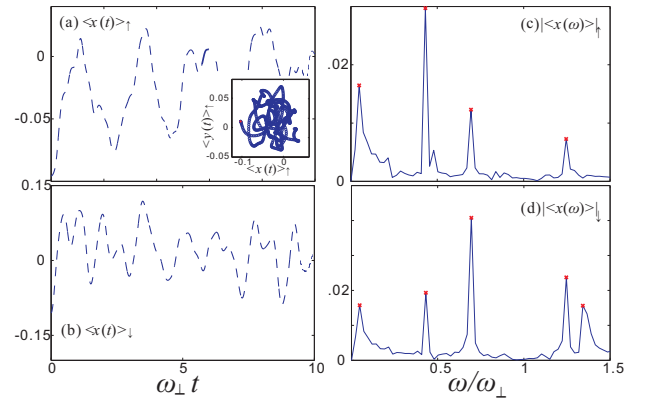


Figure 11: (color online). Parameters used: $\lambda_{SO} = 1.0, g(N-1) = 40\hbar\omega_\perp/a_\perp^2, g_{\uparrow\downarrow} = 1.1g$. (a),(b): Dynamic response of the center-of-mass coordinate in x -direction of \uparrow - and \downarrow - spin components respectively. The inset in (a) shows the dynamics of the center-of-mass coordinate over 12 trap periods and the filled (red) marker denotes the initial position. (c),(d): Corresponding single-sided amplitude spectrum of the collective coordinate.

IV. INSTABILITY ANALYSIS AND PHASE DIAGRAM

We are now ready to analyze the parameter space for the existence of half-quantum vortex state. It will become unstable with respect to increasing the interaction strength or decreasing the ratio $g_{\uparrow\downarrow}/g$. The instability could be indicated from some energy considerations and from the softening of collective density modes.

A. Superposition instability

As we mentioned earlier, for any half-quantum vortex state, $\phi(\mathbf{r}) = [\phi_{\uparrow}(\rho), \phi_{\downarrow}(\rho)e^{i\varphi}]^T/\sqrt{2\pi}$, we always have a degenerate time-reversal partner state, $\mathcal{T}\phi(\mathbf{r}) = [\phi_{\downarrow}(\rho)e^{-i\varphi}, -\phi_{\uparrow}(\rho)]^T/\sqrt{2\pi}$. There is an instability for half-quantum vortex state with respect to a superposition state, which with equal weight takes the form,

$$\phi_s(\mathbf{r}) = \frac{1}{\sqrt{4\pi}} \begin{bmatrix} \phi_{\uparrow}(\rho) + \phi_{\downarrow}(\rho)e^{-i(\varphi-\varphi_0)} \\ \phi_{\downarrow}(\rho)e^{i(\varphi-\varphi_0)} - \phi_{\uparrow}(\rho) \end{bmatrix}. \quad (38)$$

Here φ_0 is an arbitrary azimuthal angle. The energy difference between the superposition state and the half-quantum vortex state is given by,

$$\Delta E_{\text{GP}} = \frac{(g_{\uparrow\downarrow} - g)(N-1)}{4} W[\phi(\mathbf{r})]. \quad (39)$$

Therefore, if $W[\phi(\mathbf{r})] > 0$, the half-quantum vortex state is stable only when $g < g_{\uparrow\downarrow}$.

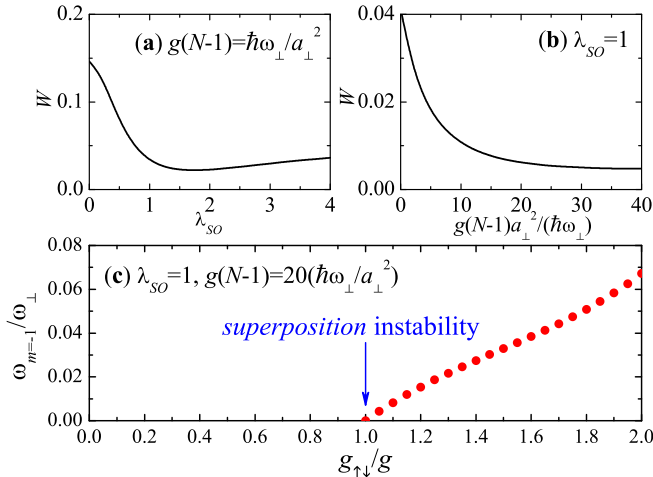


Figure 12: (color online). (a) The W -function as a function of SO coupling at $g(N-1) = \hbar\omega_{\perp}/a_{\perp}^2$ and $g_{\uparrow\downarrow} = 1.1g$. (b) The W -function as a function of interaction strength at $\lambda_{SO} = 1$ and $g_{\uparrow\downarrow} = 1.1g$. (c) The instability of the lowest dipole mode frequency $\omega_{m=-1}$ with decreasing $g_{\uparrow\downarrow}/g$ at $\lambda_{SO} = 1$ and $g(N-1) = 20\hbar\omega_{\perp}/a_{\perp}^2$.

In Figs. 12(a) and (b), we check the W -function of the half-quantum vortex state in the presence of interatomic

interactions. It always appears to be positive, though the interactions tend to decrease its absolute magnitude. Hence, there must be a quantum phase transition occurring at the isotropic point $g = g_{\uparrow\downarrow}$. Once $g > g_{\uparrow\downarrow}$, a superposition state with density pattern,

$$n_{\uparrow,\downarrow} = \frac{1}{2\pi} \left[\frac{\phi_{\uparrow}^2 + \phi_{\downarrow}^2}{2} \pm \phi_{\uparrow}\phi_{\downarrow} \cos(\varphi - \varphi_0) \right], \quad (40)$$

becomes preferable. The 2D contour plot of this density pattern with $\varphi_0 = 0$ is schematically shown in the inset of Fig. 1 (in the phase IIA).

In general, in passing the quantum phase transition point, we would observe softening of a particular mode frequency. As the superposition state involves a time-reversal state with angular momentum $m = -1$, the lowest dipole mode with $m = -1$ may become unstable. In Fig. 12(c), we plot the lowest dipole mode frequency $\omega_{m=-1}$ as a function of $g_{\uparrow\downarrow}/g$ at $\lambda_{SO} = 1$ and $g(N-1) = 20\hbar\omega_{\perp}/a_{\perp}^2$. Indeed, with decreasing $g_{\uparrow\downarrow}/g$, the mode frequency $\omega_{m=-1}$ decreases and approaches to zero exactly at the phase transition point.

B. Instability to high-order angular momentum components

There is another instability for the half-quantum vortex state, occurring with increasing the interatomic interactions. With sufficiently large interactions, we anticipate that the state with high-order azimuthal angular momentum will energetically become favorable. For example, let us consider a condensate state with an azimuthal angular momentum $m = 1$ (the 3/2-quantum vortex state), which has the form,

$$\phi_{m=1}(\mathbf{r}) = \frac{1}{\sqrt{2\pi}} \begin{bmatrix} \phi_{\uparrow}(\rho)e^{i\varphi} \\ \phi_{\downarrow}(\rho)e^{i2\varphi} \end{bmatrix}. \quad (41)$$

The GP energy of this state can be obtained by solving the GPE equation as before, except that we need to take $R_{k1}(\rho)$ and $R_{k2}(\rho)$ as the expansion functions for $\phi_{\uparrow}(\rho)$ and $\phi_{\downarrow}(\rho)$, respectively. Its degenerate time-reversal partner state has an azimuthal angular momentum $m = -2$.

It is easy to see from Fig. 13(a) that beyond a critical interaction strength the condensate state with $m = 1$, $\phi_{m=1}(\mathbf{r})$, is lower in energy than the half-quantum vortex state, $\phi_{m=0}(\mathbf{r})$. We note, however, that the critical interaction strength determined in this way is not accurate, as a superposition state of $\phi_{m=0}(\mathbf{r})$ and $\phi_{m=1}(\mathbf{r})$ may already become energetically more preferable than $\phi_{m=1}(\mathbf{r})$ at a smaller interaction strength.

An accurate determination of the threshold could be obtained by monitoring the instability in a particular collective mode. As the condensate state may preserve a well-defined parity, we find that the instability occurs in the lowest quadrupole mode with $m = -2$. In

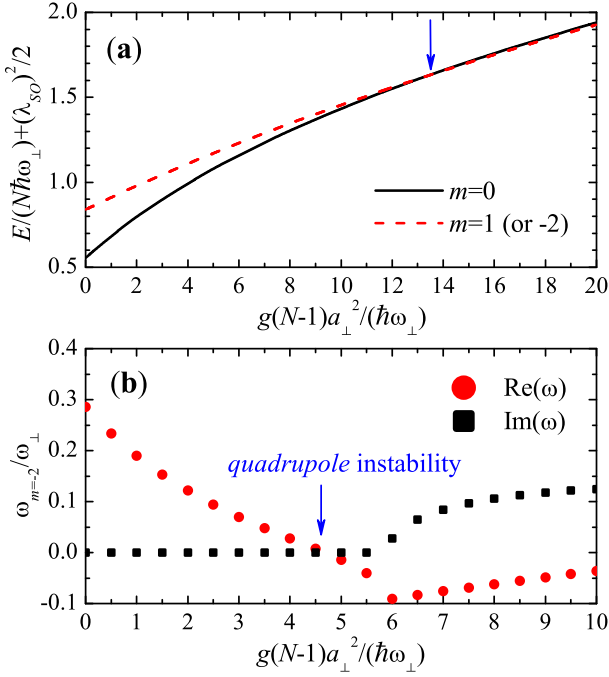


Figure 13: (color online). (a) GP energy of the 3/2-quantum vortex state $\phi_{m=1}(\mathbf{r})$ and of the half-quantum vortex state $\phi_{m=0}(\mathbf{r})$ as a function of interaction strength at $\lambda_{SO} = 2$ and $g_{\uparrow\downarrow}/g = 1.1$. Beyond a critical interaction strength as indicated by an arrow, $\phi_{m=1}(\mathbf{r})$ becomes energetically favorable. (b) The corresponding lowest quadrupole mode frequency $\omega_{m=-2}$. It becomes unstable beyond a threshold g_c .

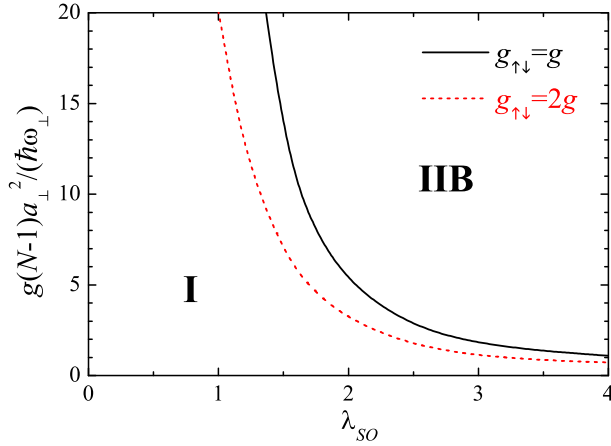


Figure 14: (color online). Phase diagram at $g_{\uparrow\downarrow} = g$ and $g_{\uparrow\downarrow} = 2g$. The critical interaction strength has been shown as a function of SO coupling.

Fig. 13(b), we report the lowest quadrupole mode frequency $\omega_{m=-2}$ as a function of the interaction strength. As the interaction increases, the real part of mode frequency decreases down to zero and then, the imaginary part becomes positive, indicating clearly that this mode will exponentially grow if the condensate is initially in the half-quantum vortex configuration. The condensate then

starts to involve high-order angular momentum components. The critical interaction strength g_c can be simply determined from the softening of the mode frequency, $\omega_{m=-2}(g = g_c) = 0$.

In Fig. 14, we present critical interacting strength as a function of SO coupling at $g_{\uparrow\downarrow} = g$ and $g_{\uparrow\downarrow} = 2g$. The solid line at the isotropic point $g_{\uparrow\downarrow}/g$ has been recently calculated by Xiang-Fa Zhou and Congjun Wu by using an imaginary time evolution method [13, 28]. Our results are in excellent agreement with theirs. We find that at smaller SO coupling the critical interaction strength decreases rapidly with increasing $g_{\uparrow\downarrow}/g$.

C. Instability against anisotropy in SO coupling strength

So far we have focused our attention on the half-quantum vortex state supported by an isotropic 2D harmonic trap subject to an isotropic Rashba SO coupling. Here we discuss the effect of the anisotropy in SO coupling strength λ_R on the stability of half-quantum vortex state. The effect of the trap anisotropy will be discussed in the next subsection. In the context of ultracold gases, anisotropic Rashba spin-orbit coupled was first discussed in Ref. [6] and the coupled GP equations were solved for a many-body system in the absence of the trap and in the restricted scenario when $g_{\uparrow\downarrow} = g$. Here, we move beyond these restrictions and discuss the ground state of the system. We write the SO coupling term in the form $\mathcal{V}_{SO} = -i(\lambda_y \hat{\sigma}_x \partial_y - \lambda_x \hat{\sigma}_y \partial_x)$, where λ_x, λ_y are SO coupling strengths in the two perpendicular directions. By including this SO coupling term and solving the coupled GP equations under the Hamiltonian as given in Eq. (3) using the TSSP technique, we obtain the ground state wavefunction at various values of anisotropy in SO coupling represented by λ_x/λ_y . In Fig. 15, we plot the corresponding ground state density profiles of \downarrow -spin component for an SO coupling strength of $\lambda_x = 4.0$, and for various values of λ_x/λ_y .

We see from Fig. 15(a) that the half-quantum vortex state is indeed the ground state (already mentioned in Fig. 1(b)) for the parameter set: $g(N-1) = 0.1\hbar\omega_{\perp}/a_{\perp}^2$, $g_{\uparrow\downarrow}/g = 1.1$, $\lambda_x = 4.0$ and $\lambda_x/\lambda_y = 1.0$. We shall now analyze the pattern in which the density profile changes with anisotropy in SO coupling strength as shown in Fig. 15(b)-(d). It is evident from the density distributions in Fig. 15, that the half-quantum vortex state is unstable even against small anisotropy in SO coupling strength. Adopting a similar method as presented in Ref. [29], we analyze this systematically by expanding the wavefunction of \downarrow -component in an orthogonal basis set of the form: $\Phi_{\downarrow}(\rho) = \sum_n f_n(\rho) e^{i(2n+1)\varphi}$, where n measures the vorticity, and $f_n(\rho)$ absorbs the n th mode's contribution in radial direction. We quantify the weights of the wavefunction in the n th mode by computing $a_n = \int d\rho |f_n(\rho)|^2$. In Fig. 16, we plot the weights a_n relative to a_0 computed for half-quantum vortex state

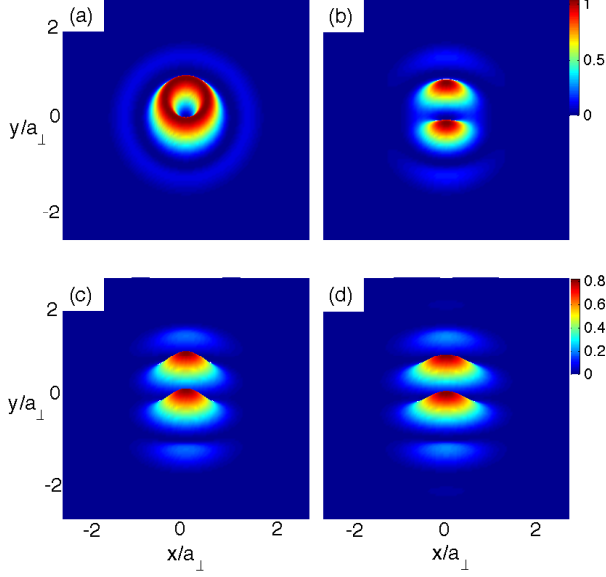


Figure 15: (Color online) Plot of the ground state density profiles of \downarrow -spin component for the parameter set: $g(N-1) = 0.1\hbar\omega_{\perp}/a_{\perp}^2$, $g_{\uparrow\downarrow}/g = 1.1$, $\lambda_x = 4.0$, but with varying ratios of λ_x/λ_y . (a) Isotropic case: $\lambda_x/\lambda_y = 1.0$, (b) $\lambda_x/\lambda_y = 1.01$, (c) $\lambda_x/\lambda_y = 1.05$, (d) $\lambda_x/\lambda_y = 1.1$. Viewing angle is slightly tilted for aesthetic purposes.

with $\lambda_x/\lambda_y = 1.0$. As we would expect, for this isotropic case, $a_0 = 1$ and $a_n = 0$ for $n \neq 0$. As anisotropy in SO coupling strength increases, more and more $n \neq 0$ components will be mixed into the ground state.

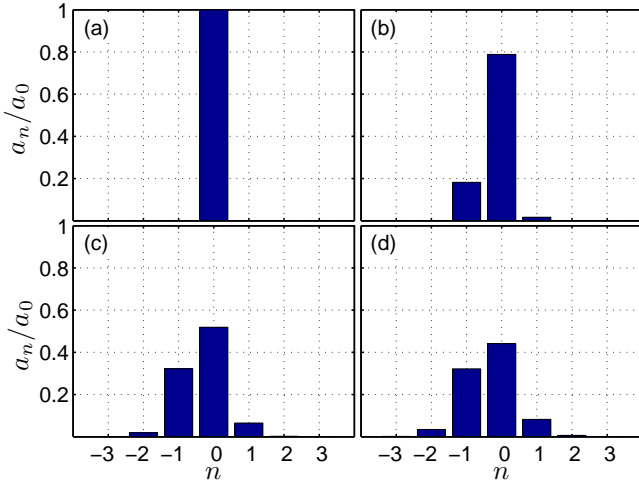


Figure 16: (Color online) Plot of the weights of ground-state wavefunction of \downarrow -spin component - corresponding to the density profiles in Fig. 15 - in the n th mode. The weights are normalized with respect to a_0 computed for half-quantum vortex state with $\lambda_x/\lambda_y = 1.0$. (a) Isotropic case: $\lambda_x/\lambda_y = 1.0$, (b) $\lambda_x/\lambda_y = 1.01$, (c) $\lambda_x/\lambda_y = 1.05$, (d) $\lambda_x/\lambda_y = 1.1$.

D. Instability to anisotropy in trap potential

Now we examine the effect of anisotropy in the trapping potential, but with isotropic SO coupling, on the stability of half-quantum vortex state. We write the trapping potential in the form $V(x, y) = M(\omega_x^2 x^2 + \omega_y^2 y^2)/2 = M\omega_{\perp}^2(x^2 + f_y^2 y^2)/2$, where $\omega_x = \omega_{\perp}$, $\omega_y = f_y \omega_{\perp}$ are trapping frequencies in x - and y -directions respectively. We again obtain the ground state wavefunctions at various values of f_y by solving the coupled GP equations using the TSSP technique. In Fig. 17, we plot the corresponding ground state density profiles of \downarrow -spin component for an SO coupling strength of $\lambda_{SO} = 4.0$, and for various values of trap anisotropy ranging from 0 to 10%.

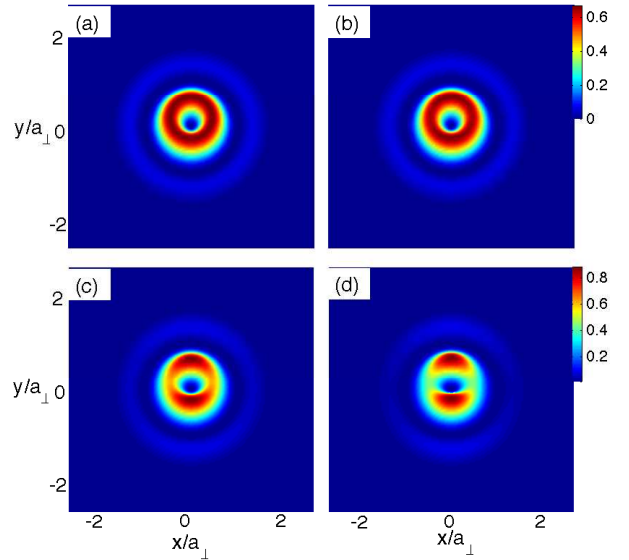


Figure 17: (Color online) Plot of the ground state density profiles of \downarrow -spin component for the parameter set: $\lambda_{SO} = 4.0$, $g(N-1) = 0.1\hbar\omega_{\perp}/a_{\perp}^2$, $g_{\uparrow\downarrow}/g = 1.1$, but with varying ratios of $f_y = \omega_y/\omega_x$. (a) Isotropic case: $f_y = 1.0$, (b) $f_y = 1.01$, (c) $f_y = 1.05$, (d) $f_y = 1.1$. Viewing angle is slightly tilted for aesthetic purposes.

We see from Fig. 17(a) that the half-quantum vortex state is indeed the ground state (already mentioned in Fig. 15(a)) for the parameter set: $\lambda_{SO} = 4.0$, $g(N-1) = 0.1\hbar\omega_{\perp}/a_{\perp}^2$, $g_{\uparrow\downarrow}/g = 1.1$. We shall now analyze the pattern in which the density profile changes with trap anisotropy Fig. 17(b)-(d). It is evident from the density distributions in Fig. 17, that the vortex core becomes increasingly anisotropic with increasing f_y . We analyze this systematically by expanding the wavefunction of \downarrow -component in an orthogonal basis set and quantifying the weights in the n th mode by a_n , as mentioned in Sec. IV C. In Fig. 18, we plot the weights a_n relative to a_0 computed for half-quantum vortex state with $f_y = 1.0$. As we would expect, for the isotropic case with $f_y = 1.0$, $a_0 = 1$ and $a_n = 0$ for $n \neq 0$. As trap anisotropy in-

creases, we observe that the ground state is a mixture of $n \neq 0$ components as well. Nevertheless, we see that the trap anisotropy has a much smaller effect on the half-quantum vortex state than the anisotropy in the SO coupling strength.

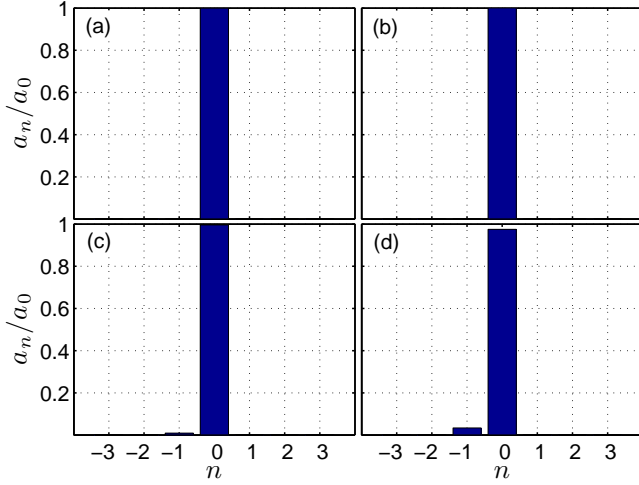


Figure 18: (Color online) Plot of the weights of ground-state wavefunction of \downarrow -spin component - corresponding to the density profiles in Fig. 17 - in the n th mode. The weights are normalized with respect to a_0 computed for half-quantum vortex state with $f_y = 1.0$. (a) Isotropic case: $f_y = 1.0$, (b) $f_y = 1.01$, (c) $f_y = 1.05$, (d) $f_y = 1.1$.

V. CONCLUSIONS

In summary, we have investigated systematically the ground condensate state of a spin-orbit coupled spin-1/2 Bose gas confined in two-dimensional harmonic traps. The density distributions and collective density excitations have been obtained respectively by solving the Gross-Pitaevskii equation and Bogoliubov equation, which are generalized to include the spin-orbit coupling.

We have found that:

(1) The condensate is in a half-quantum vortex state, if the intra-species interaction g is smaller than inter-species interaction $g_{\uparrow\downarrow}$ and, if the interaction strength is below a threshold g_c . We have calculated the threshold by monitoring the unstable quadrupole mode with an azimuthal angular momentum $m = -2$. A phase diagram for the half-quantum vortex state is therefore determined, as given in Figs. 1 and 14.

(2) The half-quantum vortex state (the phase I) will turn into a superposition of two degenerate half-quantum vortex states (the phase IIA) if $g > g_{\uparrow\downarrow}$ and will start to involve high-order angular momentum components (the phase IIB) if $g > g_c$, where g_c depends critically on the ratio $g_{\uparrow\downarrow}/g$. The half-quantum vortex state is unstable against small anisotropy in SO coupling strength and large anisotropy in trapping potential. The state tends to be a superposition of higher angular momentum states.

(3) In the presence of spin-orbit coupling, the behavior of collective density modes becomes complicated. In particular, the breathing mode with $\omega = 2\omega_{\perp}$ and the dipole mode with $\omega = \omega_{\perp}$ are no longer the exact solutions of the many-body system.

(4) The condensate wave-functions in the phases IIA and IIB are yet to be determined using the time-splitting spectral method for GPE. These wave-functions break the rotational symmetry. We anticipate that interesting density patterns will emerge in the limit of very large interatomic interactions. This is to be explored in future studies.

Acknowledgments

We would like to thank Congjun Wu and Xiang-Fa Zhou for useful discussions. BR thanks Lin Dong and Hong Lu for useful discussions. HH and XJL was supported by the ARC Discovery Projects No. DP0984522 and No. DP0984637. HP is supported by the NSF, the Welch Foundation (Grant No. C-1669) and the DARPA OLE program.

-
- [1] M. H. Anderson, J. R. Ensher, M. R. Matthews, C. E. Wieman, and E. A. Cornell, *Science* **269**, 198 (1995).
 - [2] K. M. O'Hara, S. L. Hemmer, M. E. Gehm, S. R. Granade, and J. E. Thomas, *Science* **298**, 2179 (2002).
 - [3] H. Hu, X.-J. Liu, and P. D. Drummond, *New J. Phys.* **12**, 063038 (2010).
 - [4] M. Greiner, O. Mandel, T. Esslinger, T. W. Hänsch, and I. Bloch, *Nature* **415**, 39 (2002).
 - [5] Y.-J. Lin, K. Jiménez-García, and I. B. Spielman, *Nature (London)* **471**, 83 (2011).
 - [6] T. D. Stanescu, B. Anderson, and V. Galitski, *Phys. Rev. A* **78**, 023616 (2008).
 - [7] M. Merkl, A. Jacob, F. E. Zimmer, P. Ohberg, and L. Santos, *Phys. Rev. Lett.* **104**, 073603 (2010).
 - [8] C. Wang, C. Gao, C.-M. Jian, and H. Zhai, *Phys. Rev. Lett.* **105**, 160403 (2010).
 - [9] T.-L. Ho and S. Zhang, *Phys. Rev. Lett.* **107**, 150403 (2011).
 - [10] Y. Zhang, L. Mao, and C. Zhang, eprint arXiv:1102.4045 (to appear in *Phys. Rev. Lett.*).
 - [11] Z. F. Xu, R. Lu, and L. You, *Phys. Rev. A* **83**, 053602 (2011).
 - [12] T. Kawakami, T. Mizushima, and K. Machida, *Phys. Rev. A* **84**, 011607(R) (2011).
 - [13] C. Wu, I. Mondragon-Shem, and X.-F. Zhou, *Chin. Phys. Lett.* **28**, 097102 (2011).
 - [14] X.-Q. Xu and J. H. Han, *Phys. Rev. Lett.* **107**, 200401 (2011).

- [15] X.-F. Zhou, J. Zhou, and C. Wu, eprint arXiv:1108.1238.
- [16] J. Radic, T. Sedrakyan, I. B. Spielman, and V. Galitski, eprint arXiv:1108.4212.
- [17] H. Hu, B. Ramachandhran, H. Pu, and X.-J. Liu, eprint arXiv:1108.4233 (to appear in Phys. Rev. Lett.).
- [18] S. Sinha, R. Nath, and L. Santos, eprint arXiv:1109.2045 (to appear in Phys. Rev. Lett.).
- [19] T. Yefsah, R. Desbuquois, L. Chomaz, K. J. Günter, and J. Dalibard, eprint arXiv:1106.0188.
- [20] A. Griffin, Phys. Rev. B **53**, 9341 (1996); P. A. Ruprecht, M. Edwards, K. Burnett, and C. W. Clark, Phys. Rev. A **54**, 4178 (1996); H. Pu and N. P. Bigelow, Phys. Rev. Lett. **80**, 1134 (1998).
- [21] X.-J. Liu, H. Hu, A. Minguzzi, and M. P. Tosi, Phys. Rev. A **69**, 043605 (2004).
- [22] M. M. Salomaa and G. E. Volovik, Phys. Rev. Lett. **55**, 1184 (1985).
- [23] H. Pu and N. P. Bigelow, Phys. Rev. Lett. **80**, 1130 (1998).
- [24] W. Bao, D. Jaksch and P. A. Markowich, J. Comp. Phys **187**, 318 (2003); W. Bao, Multiscale Model. Simul. **2**, 210 (2004).
- [25] H. Wang, J. Comput. Appl. Math. **205**, 88 (2007).
- [26] D. A. W. Hutchinson, E. Zaremba, and A. Griffin, Phys. Rev. Lett. **78**, 1842 (1997).
- [27] P. Ohberg and S. Stenholm, Phys. Rev. A **59**, 3890 (1999).
- [28] X.-F. Zhou and C. Wu, unpublished.
- [29] S. Yi, and H. Pu, Phys. Rev. A **73**, 061602(R) (2006).